Analysis and Design of Bidirectional Parallel-Series DAB-Based Converter

Emanuel Serban, *Senior Member, IEEE*, Cosmin Pondiche, *Member, IEEE*, and Martin Ordonez, *Member, IEEE*

***Abstract*—Unprecedented expansion of renewable, energy storage, and fast charger system applications has diversified the bidirectional converter designs over the past decade. This article presents a new dual-active bridge (DAB) converter topology, which employs parallel and series switches arrangements for low-voltage bridge configurations. The additional switch inclusion provides high dc conversion gain, which enables attractive fast charger applications. The performance of the proposed DAB-based converter with wide dc range has been investigated through several design techniques and comparisons. The use of use of silicon carbide (SiC) devices in higher power conversion significantly improves switching losses. However, unsupervised design will result in significant switching losses and increased electromagnetic emissions. Since the DAB-based converter's high switching frequency allows operation with smaller magnetics, the system stray capacitance plays a critical role. The common-mode current propagated through the system's stray capacitance generates undesired electromagnetic interferences (EMI) and impacts the soft-switching achievable range. To overcome the common-mode current circulation issue, design solutions have been employed to reduce the emergence of system stray capacitance. A harmonic analysis is further discussed along with evaluation of transformer design comparisons. The experimental results show the performance of the DAB-based converter in bidirectional operation and improved common mode current generation with respect to EMI emissions. The simulation and experimental results have been performed using a 5 kW rated power DAB-based converter with SiC power semiconductors.**

***Index Terms*—Bidirectional dc–dc converter, common-mode current, dc conversion gain, dual active bridge, electromagnetic compatibility, parallel-series DAB-based converter.**

I. INTRODUCTION

MODERN applications of electric vehicles chargers, solar photovoltaics (PV), and 5G wireless dc networks require the integration of advanced power electronic converters to energy storage systems. The dual active bridge (DAB) dc–dc isolated converter shows significant advantages including bidirectional power flow, soft-switching operation, and high-power density. The DAB topology and its advantages have been introduced and discussed in the literature [1], [2]. The issues of the DAB converter achieving zero voltage switching (ZVS) and reactive power due to circulation currents has also been discussed ([3], [4], [5], [6], [7], [8], [9]). The converter topology arrangements with bridge parallel input–output structure for higher current operation can be achieved [10], [11], [12], [13], [14]. Modular dc–dc converters and input–output terminals can be configured with the combination of input-parallel output parallel, input-parallel output-series [15]. The parallel bridge input and series output transformer winding connection provides the advantage of current circulation elimination between parallel bridges [16], [17], [18], [19].

The stray capacitance in the galvanically isolated converters with high-frequency transformers can lead to insulation deterioration, early failures, and undesired electromagnetic emissions. The drawbacks of common-mode voltage in DAB converters have been investigated with analytical models and compared with different modulation strategies. For example, the dc input and the converter ac output are decoupled during the converter zero state to reduce the fluctuations of the common-mode voltages [18], [19], [20], [21], [22], [23]. However, additional power devices are required, leading to overall increased converter cost. The power inductor can be placed in each of two high carry current paralleled bridges [24], consequently with the construction disadvantage of two inductors rated for high current. The topology arrangement can be further improved by placing the power inductor in the high-voltage side with lower current rating, series connected between the two transformer windings.

Fig. 1 shows the conventional DAB topology 1) and the proposed parallel-series DAB-based architecture derivation 2) with two parallel-LV full-bridge approach to allow half-current distribution in a high-power design and configurable output voltage. The LV stage employs parallel switches (Q_{p1} , Q_{p2}) and a series switch (Q_s) to allow flexible voltage configuration. The DAB-based topology shown in Fig 1(b) has an increased number of components compared with the conventional topology. However, the DAB-based converter allows higher current operation in the design requirements for high conversion ratio between input–output. As shown in Fig. 1(c), the proposed DAB-based topology allows double voltage range extension ($V_n + \Delta V_{ext}$) thanks to the parallel-series switch combination. This significant high-gain advantage expands the ranges of applications for the DAB-based converters.

The common-mode current (CMC) circulation has undesired negative effects, such as increased electromagnetic emissions,

---

Manuscript received 23 November 2022; revised 26 February 2023; accepted 14 April 2023. Date of publication 2 May 2023; date of current version 21 June 2023. Recommended for publication by Associate Editor T. Qian. *(Corresponding author: Emanuel Serban.)*

Emanuel Serban and Cosmin Pondiche are with the Department of, Energy Systems, Enersys Inc., Burnaby, BC V5J 5M4, Canada (e-mail: emanuel.serban@ieee.org; cpondiche@yahoo.ca).

Martin Ordonez is with the Department of Electrical and Computer Engineering, University of British Columbia, Vancouver, BC V6T 1Z4, Canada (e-mail: mordonez@ieee.org).

Color versions of one or more figures in this article are available at https://doi.org/10.1109/TPEL.2023.3272336.

Digital Object Identifier 10.1109/TPEL.2023.3272336

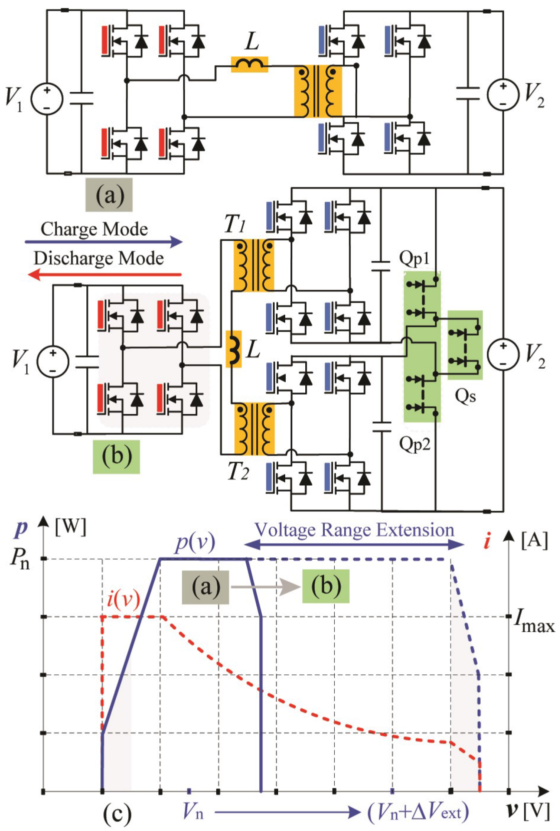

Fig. 1. Bidirectional dual-active bridge topologies. (a) Conventional topology. (b) Proposed parallel-series DAB-based converter. (c) Voltage extension range with the proposed architecture.

decrease of signal-to-noise ratio with a direct impact on converter stability, and transformer saturation. Therefore, the DAB-based CMC mitigation has been addressed in this article with a proposed design methodology. The main contributions of this article are 1) an introduction of the DAB-based converter with parallel-series LV-bridge configuration for high dc conversion gain (doubled compared to conventional topology), 2) harmonics analysis and design with reduced stray capacitance, and 3) the converter's performance analysis in bidirectional power flow with reduced common-mode current circulation and soft-switching devices operation for high efficiency operation. The rest of this article is organized as follows. Section II introduces the proposed DAB-based converter topology with wide dc range. Section III analyses the converter's harmonics and improvements in common-mode current generation. The experimental validation and performance of the DAB-based converter with parallel LV-bridges is examined in Section IV. Finally, Section V concludes this article.

II. PARALLEL-SERIES DAB-BASED CONVERTER TOPOLOGY DESCRIPTION

The parallel-series DAB-based converter topology is shown in Fig. 2. The DAB-based converter has been expanded to three full-bridge converters. Due to the high currents developed in the low-voltage (LV) side, the bridge is expanded to two, where each bridge channel handles half of the rated power. The current sharing of each LV bridge must be ensured to avoid volt-second imbalances of transformers T_1 and T_2, which can cause magnetics saturation. The high-voltage secondaries of transformers T_1 and T_2 are series connected, as shown in Fig. 2. The inductor L, which allows the power flow control, interconnects the series secondaries to the HV bridge. As shown in Fig. 2, the power inductor current (i_H) delivered during each switching period (T) is given by

$$\frac{di_H(t)}{dt} = \frac{v_\alpha(t) - v_\beta(t)}{L}. \tag{1}$$

The DAB-based average active power (P) generation during one switching period (T) is given by the contribution of two LV-bridges

$$P = \frac{1}{T}\int_0^T p_1(t)\,dt + \frac{1}{T}\int_0^T p_2(t)\,dt \tag{2}$$

where $p_1(t) + p_2(t) = p(t)$ is the active power delivered from the two LV-bridge converters. In charge mode, the average power can be described with the contribution of LV1 and LV2 bridges

$$P_{\text{charge}} = \frac{1}{T}\int_0^T v_\beta(t)\, i_{\text{H}}(\text{t})\, dt \tag{3}$$

and in discharge mode, the average power can be similarly described, considering the high voltage $v_\alpha(t)$, and inductor current $i_H(t)$

$$P_{\text{discharge}} = \frac{1}{T}\int_0^T v_\alpha(t)\, i_{\text{H}}(\text{t})\, dt. \tag{4}$$

The calculated active power transfer in charge, and discharge of the DAB-based converter is given by

$$P = n\frac{V_1 V_2}{2\pi f L}\delta\left(1 - \frac{|\delta|}{\pi}\right) \tag{5}$$

where $n = (2n_1)/n_2$ is the total magnetics (T_1, T_2) turns-ratio. The expression (5) shows the relationship between the active power transferred as function of the phase-shift (δ) between the HV- and LV-bridges, the converter switching frequency and the energy transfer inductance. The maximum power transfer occurs under the condition of $\frac{dP}{d\delta} = 0$ as given by

$$P_{1\max} = \frac{2n_1}{n_2} V_1 V_2 \frac{1}{8fL}. \tag{6}$$

The maximum power occurs at $\delta = \pm\pi/2$ and the phase-shift can in general be expressed as

$$\delta = \frac{\pi}{2}\left(1 - \sqrt{1 - \frac{n_2}{2n_1}\frac{8fL\,|P|}{V_1 V_2}}\right). \tag{7}$$

Fig. 2 shows the inclusion of switch $q_{sp} = \{Q_{p1}, Q_{p2}, Q_s\}$ within the proposed parallel-series DAB-converter, and it can be configured as follows:

$$q_{sp} = \begin{cases} Q_{p1} \wedge Q_{p1} = 0,\ Q_s = 1,\ if\ V_2 < V_{\text{DSmax}} \\ Q_{p1} \wedge Q_{p1} = 1,\ Q_s = 0,\ if\ V_2 \geq V_{\text{DSmax}} \end{cases}. \tag{8}$$

It is interesting to note that the switch q_{sp} state is a function of the maximum drain-source voltage V_{DSmax} of power devices

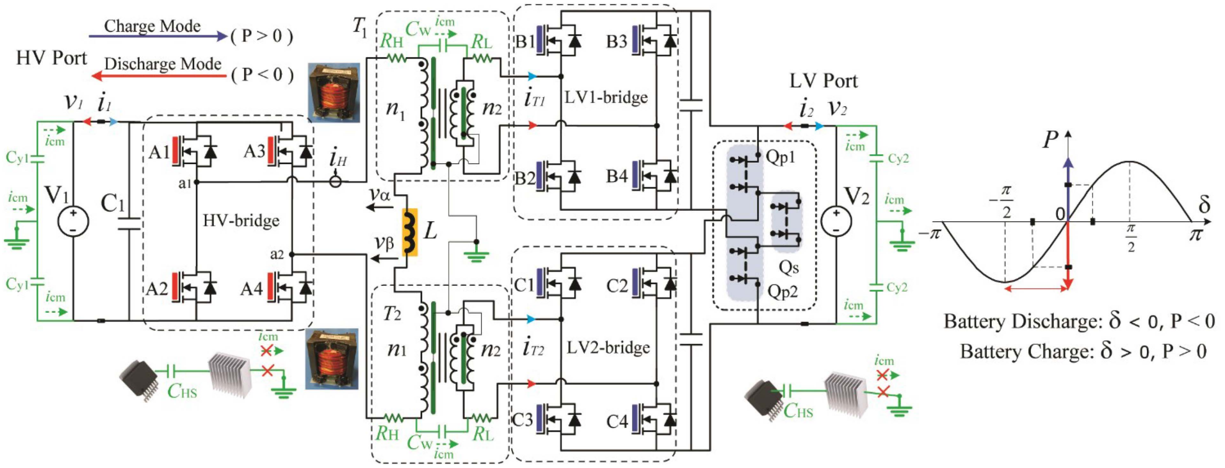

Fig. 2. Proposed parallel-series DAB-based topology designed for high DC gain and reduced common-mode current generation.

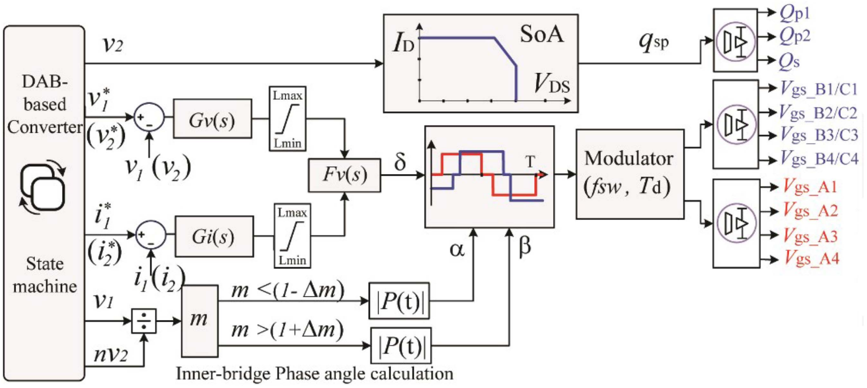

Fig. 3. Control block diagram of parallel-series DAB-based converter with wide DC voltage range capability.

$B_1 \div B_2$ and $C_1 \div C_2$, namely the maximum safe operation area.

The addition of the configurable switch q_{sp} within the energy storage DAB-converter features a wide dc operational range of the converter.

For example, in charge mode the dc conversion gain is given by

$$m = \begin{cases} n\frac{V_2}{V_1}, \; if \; q_{sp} = (Q_{p1} \wedge Q_{p2} = 1) \\ 2n\frac{V_2}{V_1}, \; if \; q_{sp} = (Q_s = 1). \end{cases} \tag{9}$$

As it can be seen from (9), the dc conversion gain is doubled, compared with the traditional approach, hence, the LV port can operate over a wide voltage range. The high converter gain, enables attractive fast charger applications, and allows converter operation over a variety of energy storage batteries.

TABLE I
TOPOLOGY COMPARISONS

Topology/ Parameter	a) Conventional DAB converter	b) Partial Parallel DAB converter	c) Parallel-Series configurable DAB-based converter
Size	Standard	Reduced	Reduced
Operating Temperature	Standard	Improved	Improved
Cost	Standard	Standard	Increased
DC Voltage Range	Standard	Standard	Doubled
Efficiency	Standard	Improved	Improved

Fig. 3 shows the control strategy implementation of the energy storage bidirectional DAB-based converter. The reference set-points for the voltage, v_1^* for discharge and v_2^* for charge, and current, i_1^* for discharge and i_2^* for charge, are configurable parameters based on the required charge or discharge modes of operation. The voltage and current regulators $(G_v(s),\ G_i(s))$ control the outer phase-shift (δ) between the HV bridge and LV-bridges to establish the power flow as per (7). With the introduction of the inner phase-angles α and β, the two-level voltage switching waveforms are transformed to three-level voltage modulation $(v_\alpha(t), v_\beta(t))$. The closed loop control structure must regulate and respond quickly to maintain the desired voltage and current setpoints $v_1^*/v_2^*,\ i_1^*/i_2^*$. The modulator control variables are the outer phase-shift δ and the inner phase-angles α and β, as shown in Fig. 3.

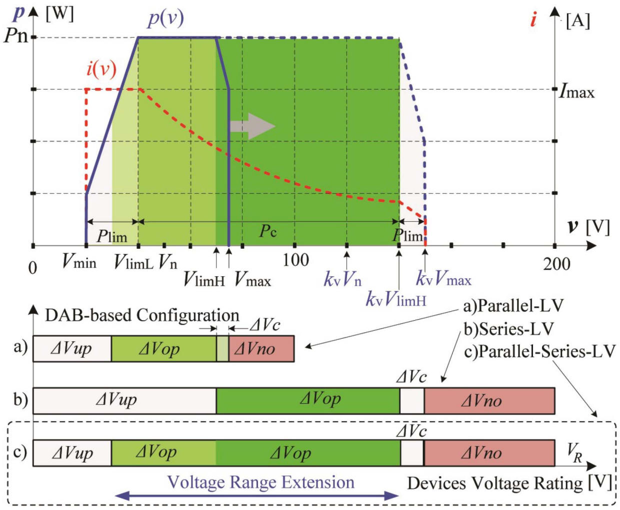

Fig. 4. Power-voltage converter characteristic: operation example of parallel-series DAB-based converter with voltage extension range.

Table I shows the comparison between a) the conventional DAB converter, b) partial parallel DAB ([17], [24]), and c) proposed parallel-series DAB-based converter. The last two mentioned converters [i.e., b) and c)] designed with two transformers and two LV-bridges, provide reduced current/power stress on components, uniformity in power loss distribution, and improved efficiency. Therefore, the power converter can be designed with reduced cooling/heatsink solutions, higher switching frequency, and operation with an increased ambient temperature (e.g., 55 °C at rated power). The proposed parallel-series DAB-based converter [i.e., c)] advantageously doubles the dc voltage range through parallel-series combination of the LV-bridges, at the expense of extra switches and higher cost.

Fig. 4 shows the power-voltage characteristics with comparisons between the following topology configurations: 1) DAB with parallel LV-bridges, 2) DAB with series LV-bridges, and 3) DAB-based parallel-series LV-bridges. Fig. 4 shows the device voltage rating V_R including the following.

1) ΔV_{up} is the under-performance range with power limited due to constant current (MOSFET device specification) and reduced voltage operation.
2) ΔV_{op} is the nominal operational range at rated power.
3) ΔV_c is the power curtailment range under power limit operation due to increased voltage (>70%) operation of the MOSFET devices.
4) ΔV_{no} is the nonoperational range of the power converter

The DAB-based power capability from Fig. 4 can be described by (10) shown at the bottom of this page, where the converter starts to operate from the minimum voltage $V_{\min}$ with maximum current $I_{\max}$ and derated power P_{lim}. Beyond the low voltage limit V_{limL} the converter can deliver nominal power P_n up to the high voltage limit V_{limH}. If the desired voltage is further increased, the converter curtails the power (P_{lim}) up to the maximum voltage $V_{\max}$. For higher voltage operation, the DAB-based converter allows the transition from parallel-LV to series-LV configuration.

If V_n is the considered converter's nominal voltage at the lower voltage range, the corresponding voltage levels are scaled-up with $k_v = (1 + \Delta V_{ext}/V_{\mathrm{n}})$, defined as extension voltage range factor (e.g., $\Delta V_{ext} = V_{\mathrm{n}}$, $k_v = 2$).

Hence, the proposed DAB-based converter allows configuration through voltage set-points for wide voltage operation. For example, this feature is highly important for fast charger applications, where different battery types are accommodated.

III. ANALYSIS AND DESIGN OF BIDIRECTIONAL DAB-BASED CONVERTER

The converter control analyzed in this article includes outer phase-shift and inner phase-angle control, which allows an additional degree of freedom for achieving soft-switching, current-stress optimization, and electromagnetic compatibility (EMC). Therefore, this provides major advantages in achieving high efficiency and reliability of power converters.

The ac voltages and inductor current contain only the odd harmonics and can be expressed based on the Fourier transformation with the following periodic function:

$$\begin{cases} v_\alpha(t) = \sum_{\mathrm{k}=0} \frac{4V_1}{(2k+1)\pi} \cos\left(\frac{(2k+1)\alpha}{2}\right) \sin\left((2k+1)\,\omega_0 t\right) \\ v_\beta(t) = \sum_{\mathrm{k}=0} \frac{4(\mathrm{n}V_2)}{(2k+1)\pi} \cos\left(\frac{(2k+1)\beta}{2}\right) \sin[(2k+1)\,(\omega_0 t - \delta)] \end{cases} . \tag{11}$$

Fig. 5 shows the fast Fourier transform (FFT) analysis at rated charge power with single phase-shift. The fundamental components of the switching waveforms, $v_{\alpha 1}(t)$ and $v_{\beta 2}(t)$, are shown in channel C1 of Fig. 5 and can be derived from (8), as follows:

$$\begin{cases} v_{\alpha 1}(t) &= \frac{4V_1}{\pi} \cos\left(\frac{\alpha}{2}\right) \sin(\omega_0 t) \\ v_{\beta 1}(t) &= \frac{4(\mathrm{n}V_2)}{\pi} \cos\left(\frac{\beta}{2}\right) \sin(\omega_0 t - \delta_1) \end{cases} . \tag{12}$$

The harmonic amplitudes of the converter switching waveforms are shown in C2 and C3 of Fig. 5. The total active power is the sum of the components generated through the odd harmonics derived from the fundamental of the switching frequency.

Fig. 6 shows the FFT analysis at rated charge power with dual phase-shift and implemented to achieve soft-switching for

---

$$p(v) = \begin{cases} 0, \text{ if } v < V_{\min} \\ V_{\min} I_{\max} \left[1 + \frac{v - V_{\min}}{V_{limL} - V_{\min}} \left(\frac{P_n}{V_{\min} I_{\max}} - 1\right)\right], \text{ if } V_{\min} \leq v < V_{limL} \\ V_n I_n, \text{ if } V_{limL} \leq v < k_v V_{limH} \\ P_n \left(1 + \frac{1}{2} \frac{v - k_v V_{limH}}{k_v V_{limH} - k_v V_{\max}}\right), \text{ if } V_{limH} \leq v < k_v V_{\max}. \\ 0, \text{ if } v \geq k_v V_{\max} \end{cases} \tag{10}$$

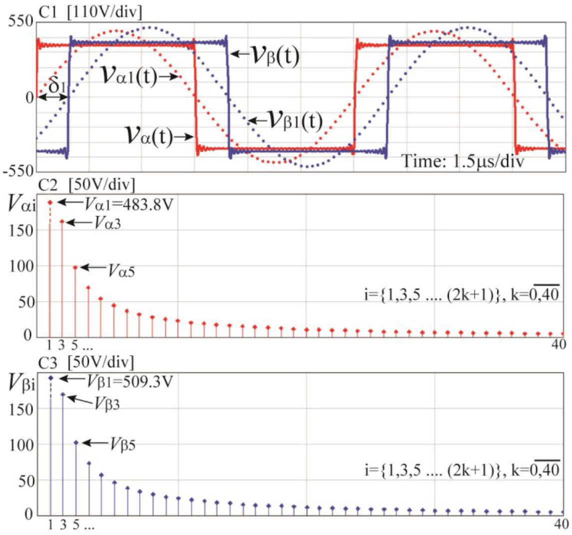

Fig. 5. FFT DAB-based converter analysis with single phase-shift control (SPS). Test conditions: charge mode, $\boldsymbol{V}_1 = 380\ \mathbf{V}$, $\boldsymbol{V}_2 = 50\ \mathbf{V}$.

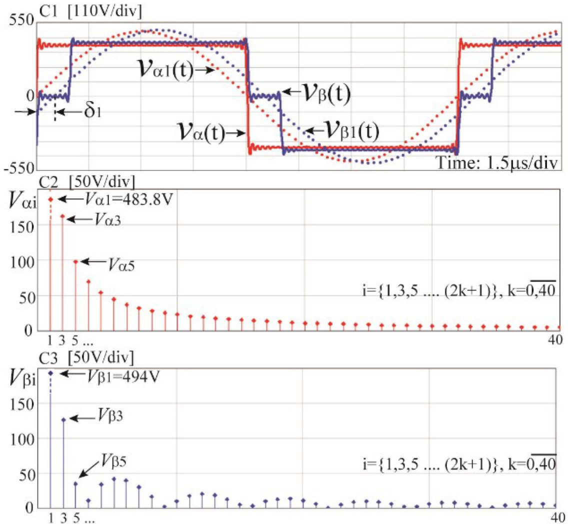

Fig. 6. FFT DAB-based converter analysis with dual phase-shift (DPS) control. Test conditions: charge mode $\boldsymbol{V}_1 = 380\ \mathbf{V}$, $\boldsymbol{V}_2 = 50$.

cases where single phase-shift ends in hard-switching. The fundamental components of the switching waveforms, $v_{\alpha 1}(t)$ and $v_{\beta 2}(t)$, respectively, are shifted by the fundamental component of phase-shift δ_1, where this angle is the main contributor to the active power generation within the converter. The soft-switching of HV and LV bridges can be considered for the following switch pairs: $(A_1,\ A_2)$, $(A_3,\ A_4)$, $\frac{B_1,\ B_2}{C_1,\ C_2}$, and $(B_3,\ B_4)/(C_3,\ C_4)$. The ZVS boundary conditions are a function of operation mode, conversion ratio (voltage amplitudes), outer phase-shift, and inner phase-angles. It is important to note that the switching characteristics of SiC devices still represent an issue due to losses generation, which will be shown in the experimental section. The energy required to achieve ZVS requires charging and discharging the output capacitance C_{oss} of the power devices and the parasitic transformer capacitance C_w and is approximated by

$$E_{\min} \geq \frac{1}{2}(2C_{\text{oss}})V_1^2 + \frac{1}{2}(C_w)V_1^2. \tag{13}$$

From (13), both stray elements, C_{oss} and C_w, respectively, disadvantageously affect the power conversion efficiency. The output capacitance C_{oss} is given by the device manufacturer, while other stray capacitances (e.g., C_w) are related to the design approach. In this article, one of the goals is the mitigation of the overall stray capacitance.

The soft-switching events of the HV and LV bridges have been achieved through the control of the inner phase-angles α and β. The phase-angles are calculated as a function of input–output voltages and output power, as shown in Figs. 3 and 7. The soft-switching can be achieved at rated input–output voltage and power using only the SPS. Dual phase shift (DPS) and triple phase-shift (TPS) have been implemented for different corner cases of converter operation, as shown in Fig. 3. The soft-switching modulation schemes with innerangles deduction have been discussed in the literature ([3], [8], [25], [26]).

It can be observed that the interwinding capacitance C_w has a direct impact on reducing the soft-switching range. One of the goals in this article is to reduce the stray transformer capacitance to improve overall converter performance. The built-in parasitic interwinding capacitance of the two transformers facilitates paths for common-mode current propagation between the LV side and the HV side. The common mode voltage developed between positive/negative conductors of the converter and the ground protective earth (PE) generates leakage currents through the equivalent total parasitic capacitance C_t. The voltage fluctuation at the positive and negative terminals becomes the generator source for the leakage currents. Its conduction path is formed through the input and output EMI capacitors (C_{y1} and C_{y2}). The CMC generation and circulation concerns the electromagnetic interference, and is given by

$$i_{\text{CM}}\ (t) = C_t\,\frac{dV_{\text{CM}}}{dt}. \tag{14}$$

As per (14), the reduction of CMC can be achieved through the reduction of both the total parasitic capacitance and the dV/dt rate of change. The total parasitic capacitance is given by

$$C_t = 2(C_W\ + C_{HS}) \tag{15}$$

where C_w and C_{HS} are the interwinding capacitance introduced by transformers T_1 and T_2, respectively, and the heatsink to power devices stray capacitance. The stray capacitance C_{HS} is developed across the selected surface mount power devices (D2PAK TO-263-7), printed circuit board and thermal interface material. Due to the relatively large overlap area between the drain-source power devices and heatsink, the stray capacitance can be considerably high. Typical designs have the heatsinks directly connected to the ground or enclosure, where the heatsinks are attached on the chassis enclosure. In this proposed design, to further reduce the total stray capacitance, the heatsink mounting is unbonded from the PE ground and the converter enclosure.

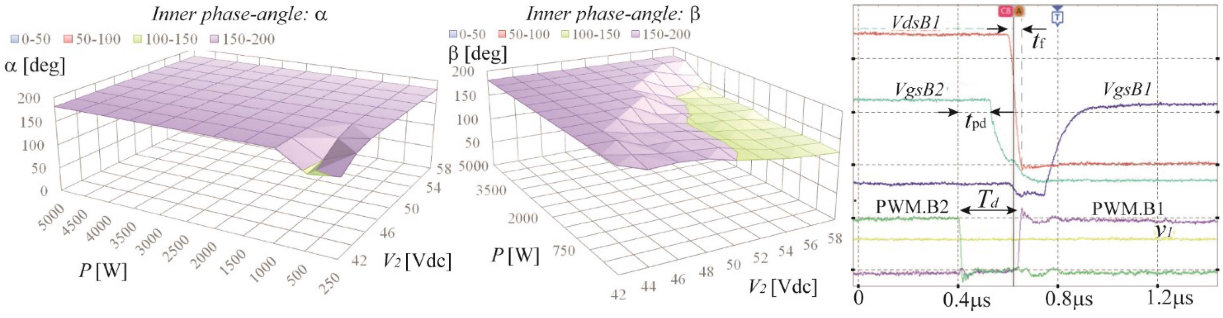

(a) (b) (c)

Fig. 7. (a) DAB-based converter control of inner phase angles α and (b) β for soft-switching operation. (c) Devices' typical switching characteristics.

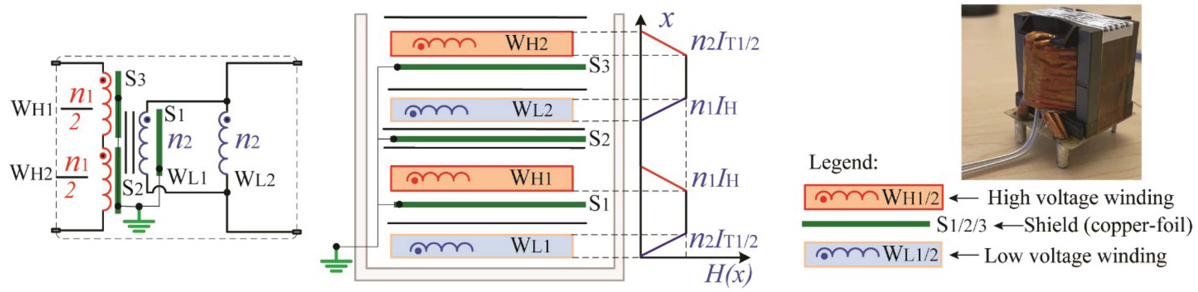

(a) (b) (c) (d)

Fig. 8. Power transformer design details with (a) schematic diagram, (b) transformer windings and layers disposition, (c) magnetomotive force diagram, and (d) prototype wire-wound shielded transformer photograph with the associated legend.

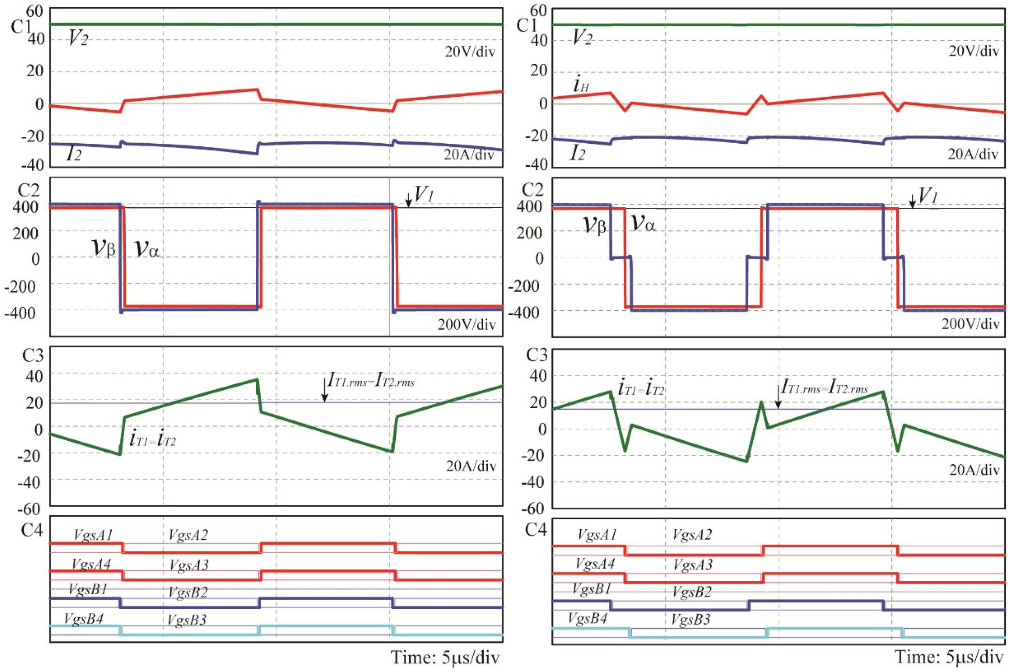

(a) (b)

Fig. 9. Simulation results of DAB-based converter in discharge mode: (a) hard-switching (SPS control) and (b) soft-switching (DPS/TPS control). Test conditions: $V_1 = 370$ V, $V_2 = 50$ V, $I_2 = 20$ A, $P_1 = 1$ kW.

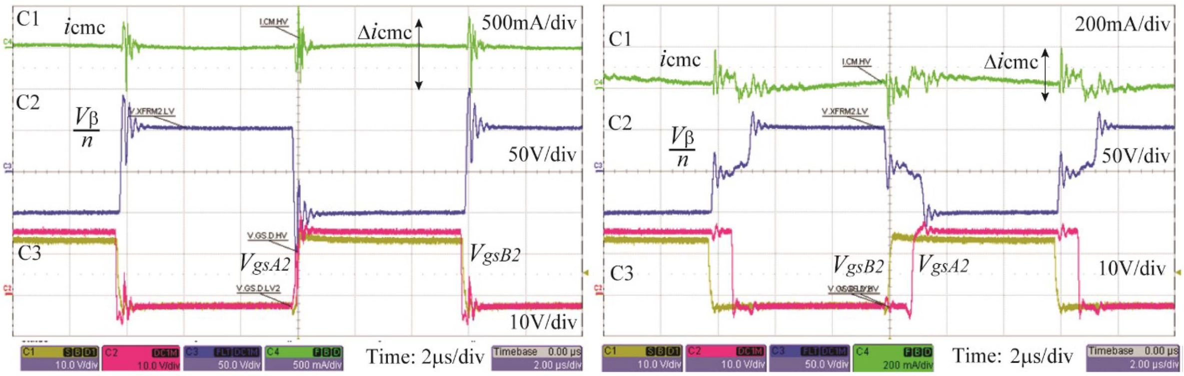

(a) (b)

Fig. 10. Common-mode current comparison: experimental results of DAB-based converter design with copper-foil (W_{L1}, W_{L2}) transformer in discharge mode ($P < 0$) under (a) hard-switching (SPS control) and (b) soft-switching (DPS/TPS control). C1 – Common-mode current i_{CMC} C2 - AC voltage measured to LV T_1 transformer terminals C3 – Gate drive voltage waveforms V_{gsA2}, V_{gsB2}. Test conditions: discharge mode, $V_1 = 370$ V, $V_2 = 50$ V, $P_1 = 1$ kW.

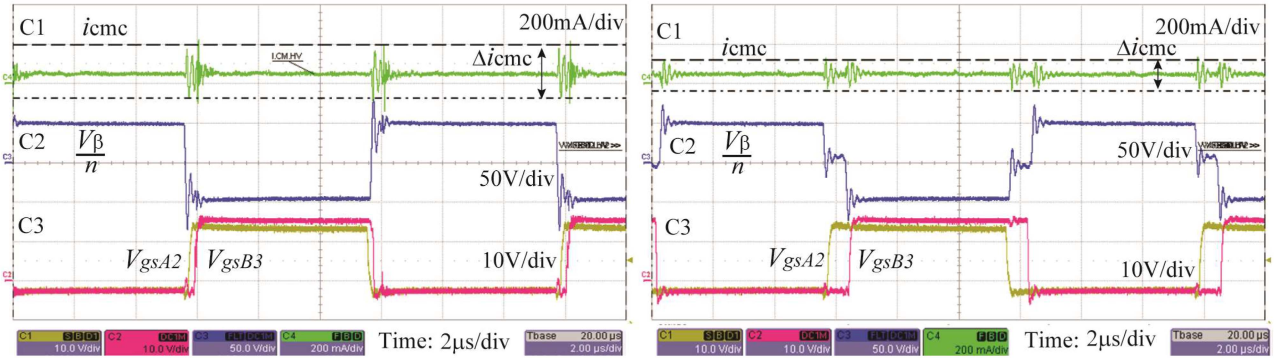

(a) (b)

Fig. 11. Common-mode current comparison: experimental results of DAB-based converter design with wire-wound (W_{L1}, W_{L2}) shielded transformer in discharge mode ($P < 0$) under (a) hard-switching (SPS control) and (b) soft-switching (DPS/TPS control). C1 – Common-mode current i_{CMC} , C2 - AC voltage measured to LV T_1 transformer terminals, C3 – Gate drive voltage waveforms V_{gsA2}, V_{gsB3}. Test conditions: $V_1 = 370$ V, $V_2 = 50$ V, $P_1 = 1$ kW.

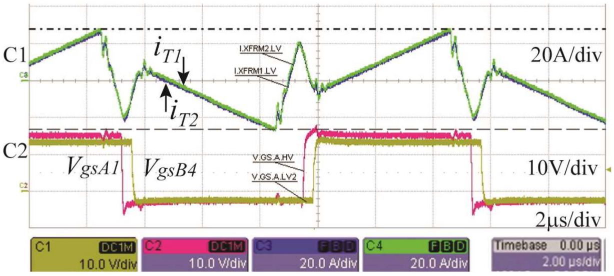

Fig. 12. DAB-based converter design with wire-wound shielded transformer experimental results in discharge mode ($\boldsymbol{P} < 0$ and control with TPS): C1 – Transformer LV currents $\boldsymbol{i_{T1}}$, $\boldsymbol{i_{T2}}$. C2 – Gate drive voltage waveforms $\boldsymbol{V_{gA1}}, \boldsymbol{V_{gB4}}$.

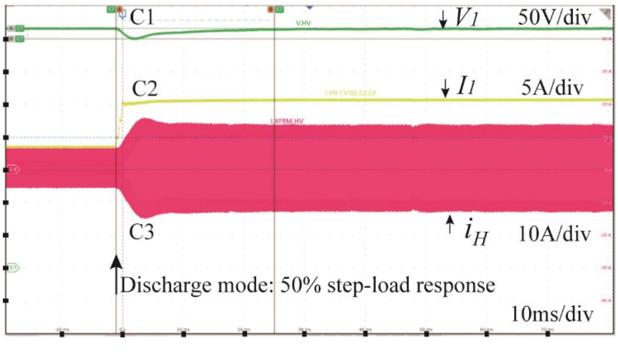

Fig. 13. DAB-based converter experimental 50% step load response in discharge mode ($\boldsymbol{P} < 0$): C1 - HV port voltage $\boldsymbol{V}_1$. C2 - HV port load current $\boldsymbol{I}_1$. C3 – Inductor current $\boldsymbol{i_H}$.

Therefore, the CMC is reduced to $i_{\text{CM}}(t) = 2C_W \frac{dV_{\text{CM}}}{dt}$ since the stray capacitance between drain-source of the power devices to PE ground has been mitigated (heatsinks are unbounded to PE). Fig. 7(a) and (b) shows the DAB-based converter's inner phase-angles distribution for the LV and HV bridges. The soft-switching can be achieved by introducing the inner phase-angles α within the HV-bridge and β within the LV1-bridge and LV2-bridge. The inner phase-angles variables are controlled as a function of the DAB power (P) range and low-voltage (e.g.,

$V_2 =\ 42 - 58$ V) range. High voltage (e.g., $V_1 =\ 380$ V) is specified at a constant operational level. As can be seen in Fig. 7(a), the inner phase-angles α within the HV-bridge need to be controlled only at light load and lower voltage range. Fig. 7(b) shows the inner phase-angles β within the LV1-bridge and LV2-bridge. In the control structure implementation, both inner phase-angles, α and β, are controlled independently, as shown in Fig. 3, and soft-switching for the end-goal of high efficiency operation is achieved. Unsupervised design can lead to mismatches in signals applied to inductor volt-second arising in both T_1 and T_2 transformers. The mismatched volt-seconds accumulate over the converter's switching operation, which may lead to significant impact through saturation of magnetic components.

The proposed DAB-based architecture considered the design of signals integrity, dead-time, and phase angles calculation to avoid dc volt-second development, which can result in power magnetics saturation.

The phase-shift variation is implemented in correlation to dead-band time, as shown in Fig 7(c). The issue of the shoot-through type of failures between the complementary gate drive signals of power devices is eliminated by maintaining the dead-band time (T_d)

$$T_d = t_{f.\max} + t_{off.\max} - t_{don.\min} + \Delta t_{pd} \tag{16}$$

where the power device specification is characterized by maximum turn-OFF switching time $t_{f.\max}$, maximum turn-OFF delay $t_{off.\max}$ (influenced by gate turn-OFF resistor $R_{\text{g.off}}$ and gate-source voltage V_{gs}), minimum turn-ON delay $t_{don.\min}$ (influenced by gate turn-OFF resistor $R_{\text{g.on}}$ and gate-source voltage V_{gs}) and gate drive circuit propagation delay $\Delta\ t_{pd} = t_{pd.\max}\ - t_{pd.\min}$. The power devices' gate signals are controlled with 50% duty-ratio while the dead-band is maintained constant during phase-angle variation.

Fig. 8 shows the power transformer design with parallel low-voltage windings and series high-voltage windings. The transformer design consists of four separate windings, namely two high-voltage (W_{H1}, W_{H2}) windings and two low-voltage (W_{L1}, W_{L2}) windings. The windings (W_{L1}, W_{L2}, W_{H1}, and W_{H2}) are separated by three shields of copper-foil layers S_1, S_2, and S_3 to achieve a low interwinding capacitance ensured by design. All the copper-foil layers (S_1, S_2, S_3) have been connected to a common potential. The magnetic cores PQ40/40 are finally assembled with the windings and copper-foil shields to complete the design. The specific construction of the high current windings W_{L1} and W_{L2} can be designed with wire-wound or copper-foil, and a comparison is provided in the following section.

IV. Simulation and Experimental Results

The simulation and experimental results are investigated with the DAB-based converter with LV-bridges configured in parallel only, and with the parameters shown in Table II. The isolation transformer designed with copper-foil has approximately five times higher interwinding capacitance than the wire-wound construction, as shown in Table II, measurements. The DAB-based converter soft-switching operation can relatively easily achieve soft-switching at rated input–output voltages and power operation.

TABLE II
Main Parameters of DAB-Based Converter

Parameter	Value
Nominal high-voltage port, V_1	380 V
Nominal low-voltage port, V_2	48 V
Single transformer (T_1/T_2) turns-ratio, n_1/n_2	4:1
Transformer (T_1/T_2) interwinding capacitance, C_w (W_{L1}, W_{L2}: wire-wound)	120 pF
Transformer (T_1/T_2) interwinding capacitance, C_w (W_{L1}, W_{L2}: copper foil)	630 pF
High/Low-voltage winding resistance, R_H/R_L	18 $m\Omega$/1.1 $m\Omega$
Power inductor, L	20 μH
Converter switching frequency, f_s	83 kHz
High-voltage bridge power devices (650V)	C3M0060065J
Low-voltage bridge power devices (100V)	IPT015N10N5
EMI Capacitors, C_{y1}, C_{y2}	20 nF, 194 nF

In this work, the experimental results are evaluated at lower power operation, in the range of 10% and 20% rated power to investigate worst-case scenarios of parallel-series DAB-based converter operation.

In this article, the experimental results are evaluated at lower power operation, in the range of 10% and 20% rated power to investigate worst-case scenarios of parallel-series DAB-based converter operation.

A. DAB-Based Converter Operation in Discharge Mode. Transformer Construction Comparison

Fig. 9 shows the key waveforms of the DAB-based converter operation in discharge mode ($P < 0$). The implementation of inner phase-angles, as shown in Fig. 9(b), allows soft-switching commutation for the power devices. In addition, under the same operating conditions, the root mean square (rms) current stress is reduced by 15% ($I_{T1.\text{rms}} = I_{T1.\text{rms}}\ = 14.9A_{\text{rms}}$ from $17.5A_{\text{rms}}$ as can be observed in Fig. 9).

Fig. 10 shows the parallel-series DAB-based converter operation using the copper-foil (W_{L1}, W_{L2}) transformer (T_1 , T_2) design. The copper-foil transformer current-mode current in hard-switching operation is shown in Fig. 9(a). As shown in Fig. 10(b), the CMC generation is reduced using the inner phase-angles from Figs. 3 and 7 for soft-switching converter operation.

Fig. 11 shows the parallel-series DAB-based converter operation with wire-wound (W_{L1}, W_{L2}) shielded transformer (T_1 , T_2) design. The results from Fig. 11(a), corresponding to hard-switching (wire-wounded) demonstrate lower CMC than Fig. 10(a) with copper-foil (W_{L1}, W_{L2}) transformer. Furthermore, the CMC is further reduced thanks to soft-switching operation, as shown in Fig. 11(b).

The measured efficiency has been improved from 91.4% (hard-switching with SPS control), to 95.6% (soft-switching

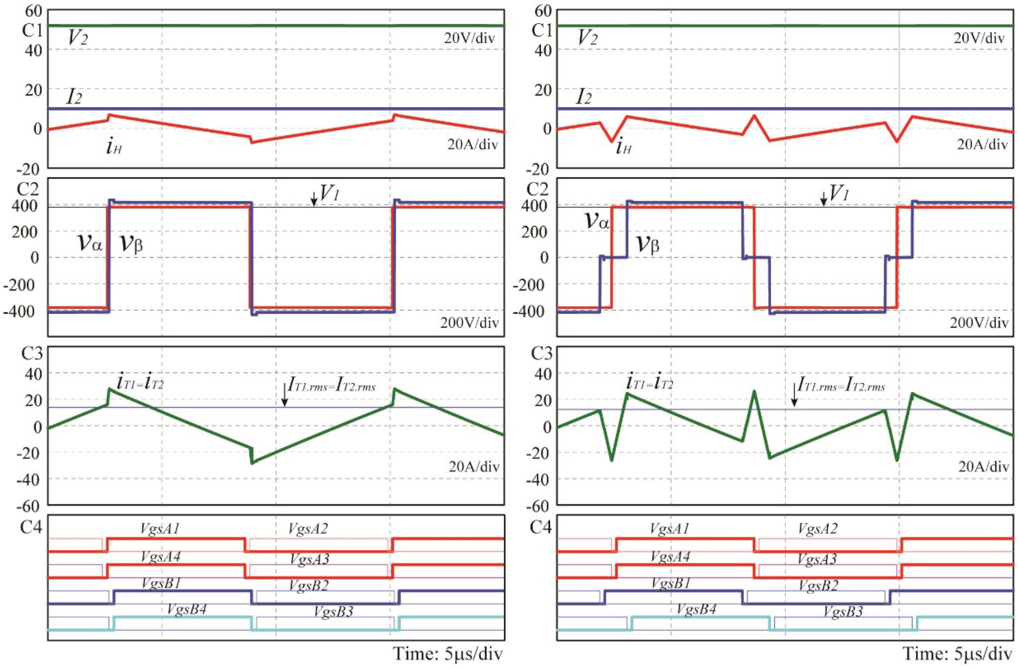

(a) (b)

Fig. 14. Simulation results of DAB-based converter in charge mode: (a) hard-switching(SPS) and (b) soft-switching (DPS/TPS). Test conditions: $V_1 = 380$ V, $V_2 = 52$ V, $I_2 = 10$ A, $P_2 = 520$ W.

TABLE III
DAB-Based Converter: Comparison Between Copper-Foil and Wire-Wound Shielded Transformer Construction

CMC measurements from Fig. 10 and Fig. 11	Δi_{cmc} $[A_{pk-pk}]$	
	Hard-switching (SPS)	Soft-switching (DPS/TPS)
Transformer (T_1/T_2) W_{L1}, W_{L2}: copper-foil	0.8	0.3
Transformer (T_1/T_2) W_{L1}, W_{L2}: wire-wound	0.25	0.15

with DPS/TPS control) which is a significant improvement. It is important to conclude that the switching characteristics of SiC devices still represent an issue due to losses generation, and they can be improved using soft-switching techniques and design techniques to reduce in the overall stray capacitance.

Table III shows the summary of common-mode current comparison between the DAB-based converter with the copper-foil and wire-wound shielded transformer construction. The symmetrical and equal currents i_{T1} and i_{T2} of the parallel low-voltage transformer windings are shown in Fig. 12. The problem of asymmetrical currents (i_{T1} , i_{T2}) in the parallel low-voltage transformer windings can lead to irreversible LV/HV bridge converter failures.

It is a common design convenience to include dc blocking capacitors in the LV and HV side of the transformer to eliminate the dc-bias and magnetics saturation issue. However, in this article, the dc-blocking capacitors were not employed for the obvious advantages of cost and size reduction. As demonstrated in Fig. 12, the identical currents are ensured by eliminating the dc-bias magnetizing current through converter controls of phase-angle generation, high efficiency gate-driver design ([27], [28]) and signal integrity since all signals are subject to effects such as distortion, noise, loss in resolution, and accuracy.

Fig. 13 shows the DAB-based converter under 50% transient step-load test in discharge mode. The closed-loop control structure (see Fig. 3) adequately regulates the voltage at the HV port under a step-load from 1 to 3.5 kW.

B. DAB-Based Converter Operation in Charge Mode. Common Mode Current Mitigation and Online Parallel to Series Power Transfer

The DAB-based converter allows bidirectional energy flow and the charge mode of operation ($P > 0$) is shown in the simulation results from Fig. 14. The implementation of inner phase-angles, as shown in Fig. 14(b), allows soft-switching commutation for the power semiconductor devices. In addition, the rms current stress is reduced by 11% [$I_{T1.\mathrm{rms}} = I_{T1.\mathrm{rms}} = 12.4A_{\mathrm{rms}}$ from $13.9A_{\mathrm{rms}}$ as can be observed in Fig. 14(a) and (b)].

The performance of the DAB-based converter with the proposed transformer design is shown in the charge mode experimental results. Figs. 15 and 16 show the experimental test results, comparing between hard-switching [see Figs. 15(a) and 16(a)] and soft-switching [see Figs. 15(b) and 16(b)] operation. At light loads of 10% of nominal power, the DAB-based converter efficiency has been significantly increased from 81.5% hard-switching commutation [see Figs. 15(a) and 16(a)] to 92%

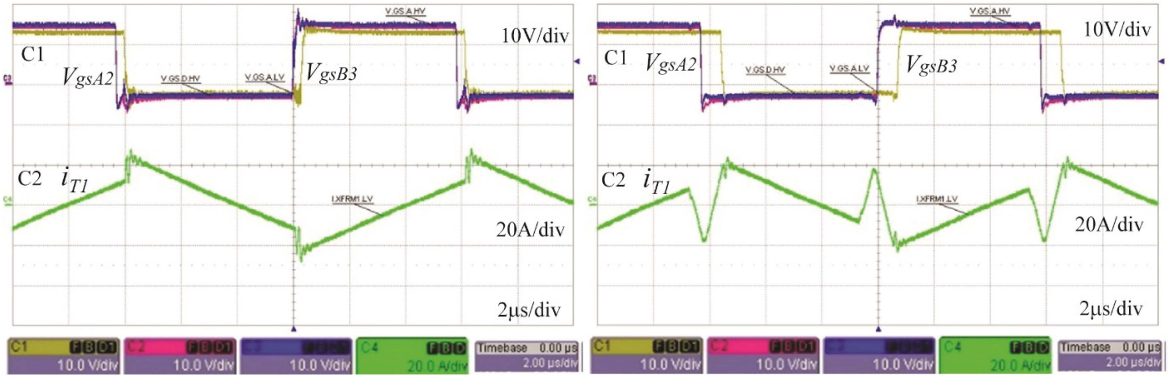

(a) (b)

Fig. 15. DAB-based converter design with wire-wound shielded transformer experimental results in charge mode ($\boldsymbol{P} > 0$): (a) hard-switching (SPS) and (b) soft-switching (DPS/TPS). C1 – Gate drive voltage waveforms $\boldsymbol{V}_{\boldsymbol{gsA}2}, \boldsymbol{V}_{\boldsymbol{gsB}3}$.C2 – Transformer LV-side current $\boldsymbol{i}_{\boldsymbol{T}1}$. Test conditions: $\boldsymbol{V}_1 = 380\mathbf{V}$, $\boldsymbol{V}_2 = 52\mathbf{V}$, $\boldsymbol{P}_2 = 520\mathbf{W}$.

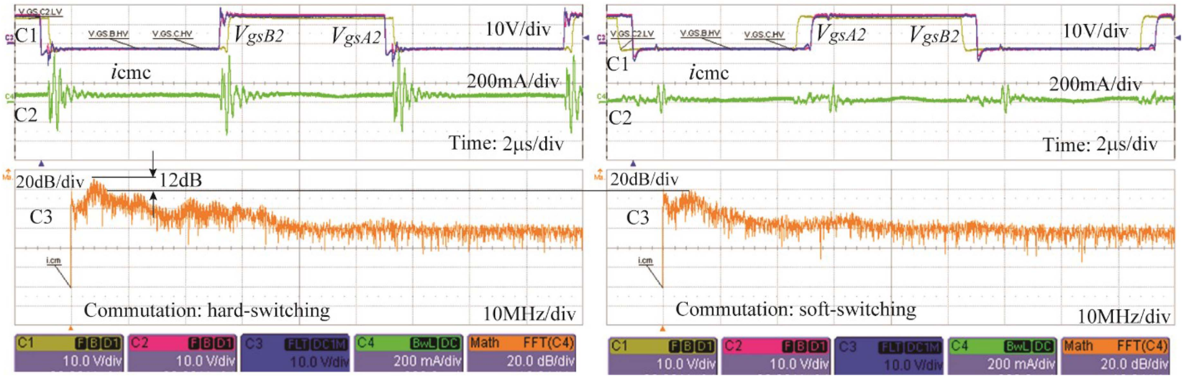

(a) (b)

Fig. 16. DAB-based converter design with wire-wound shielded transformer experimental results in charge mode ($\boldsymbol{P} > 0$): (a) hard-switching (SPS) and (b) soft-switching (DPS/TPS). C1 – Gate drive voltage waveforms $\boldsymbol{V}_{\boldsymbol{gA}4}, \boldsymbol{V}_{\boldsymbol{gB}1}$.C2 – Transformer current $\boldsymbol{i}_{\boldsymbol{T}1}$. Test conditions: $\boldsymbol{V}_1 = 380\ \mathbf{V}$, $\boldsymbol{V}_2 = 52\ \mathbf{V}$, $\boldsymbol{P}_2 = 520\ \mathbf{W}$.

soft-switching devices commutation [see Figs. 13(b) and 16(b)] operation.

Through the implementation of the soft-switching algorithm from Fig. 3 and the proposed three-layer shield transformer design, the effect of CMC emissions has been reduced by 12 dB, as can be seen in Fig. 16(a) and (b) comparisons, using the FFT frequency-domain analysis. The CMC emissions reduction has been effective in the range of up to 40 MHz, which falls mainly under the conducted emissions standards within 150 kHz to 30 MHz in the FCC and CISPR 22 requirements.

Fig. 17 shows the FFT experimental results in charge mode and under light load conditions ($V_1 = 380$ V, $V_2 = 50$ V, $P_2 = 550$ W).

The switching waveforms $v_\alpha(t)$ and $v_\beta(t)$ are shown in Fig. 17 under FFT spectrum analysis, where the ac voltages contain only the odd harmonics [as described by (8)]. Fig. 17 shows the spectrum comparison between LV-1, LV-2 bridges ac voltage operation under inner phase-angle shift $\beta = 150°$ and HV-bridge without inner phase-angle shift, i.e., $\alpha = 180°$.

Fig. 18 shows the proposed DAB-based converter performance with respect to electromagnetic interference emissions. The experimental results show the DAB-based converter's operation at five power levels, from 0.25 to 2 kW. The converter passes the class A standard limits by using the proposed transformer construction with copper shields (see Fig. 8) and soft-switching techniques (see Fig. 7).

The common-mode peak emissions are caused by the switching energy generated by the converter's power devices related to the dv_{CM}/dt rate of change. As shown in Fig. 18, the peak emissions are associated with harmonics of the fundamental switching frequency, $f_s = 83$ kHz of the power devices from Fig. 2. Therefore, the DAB-based power converter design complies for electromagnetic compatibility standard requirements by using the proposed design techniques.

Fig. 19 shows the DAB-based converter's performance with an online transition from LV-bridges parallel-connected ($q_{sp} = Q_{p1} = Q_{p2} = 0$, $Q_s = 1$) to LV-bridges series-connected ($q_{sp} = Q_{p1} = Q_{p2} = 1$, $Q_s = 0$), where the voltage is

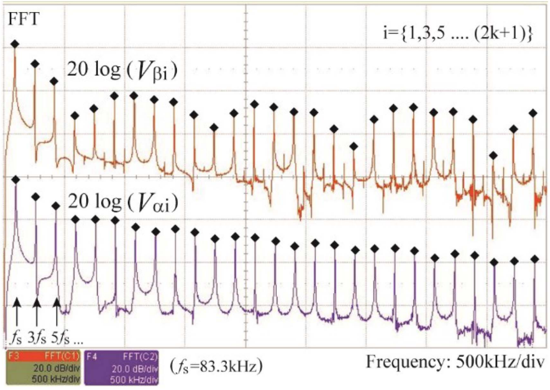

Fig. 17. FFT experimental results of DAB-based proposed converter with TPS control C1: $\boldsymbol{\beta} = 30°$ (LV-1 and LV-2 bridges) and C2: $\boldsymbol{\alpha} = 5°$ (HV-bridge). Test conditions: charge mode $\boldsymbol{V}_1 = 380\boldsymbol{V}$, $\boldsymbol{V}_2 = 50\boldsymbol{V}$, $\boldsymbol{P}_2 = 550\boldsymbol{W}$.

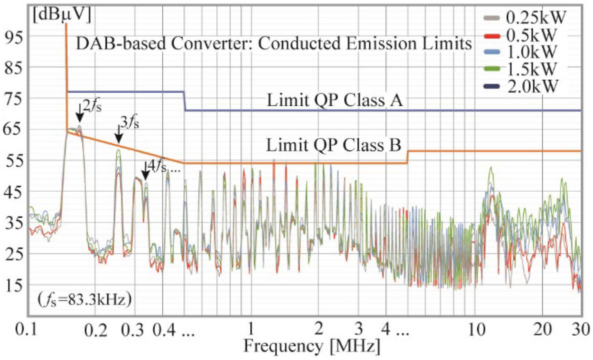

Fig. 18. Conducted emissions experimental results of DAB-based proposed converter with wire-wound shielded transformer in charge mode operation at 0.25 kW, 0.5 kW, 1 kW, 1.5 kW, and 2 kW output power.

instantly doubled from 50 to 100 V. During the transition (i.e., after t_1), with a load current I_2 programmed at $1A/\mu s$ slew rate change, the converter continues to maintain 5 kW constant power delivery. The DAB-based converter demonstrates flexible online instantaneous voltage change capability, while the dc power is constantly maintained (i.e., LV port current I_2 reduces to a half to maintain constant power operation).

C. DAB-Based Converter Efficiency Performance Measurements

Figs. 20 and 21 show the efficiency performance of the DAB-based converter in parallel LV-bridge configuration. The experimental tests were carried out in both charge and discharge modes of operation. The measurements were conducted including all the necessary auxiliary power supplies and cooling fan. The efficiency results were recorded over a wide LV voltage range $(42\text{ V} \div 58\text{ V})$ and load range from 0.25 to 5 kW, measuring a power conversion peak efficiency of 97.5%. The experimental performance validates the simulation results and demonstrates the validity of the theoretical and practical DAB-based proposed design presented in this article.

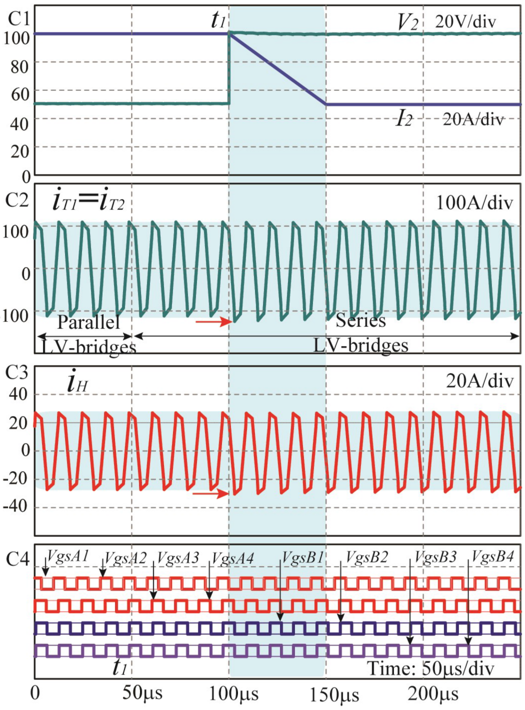

Fig. 19. DAB-based converter simulation results with online instantaneous transfer: parallel to series LV-bridges configuration, and output voltage change $50\text{ V} \rightarrow 100\text{ V}$. Test conditions: charge mode $V_1 = 380\text{ V}$, $V_2 = 50\text{ V} \rightarrow 100\text{ V}$, $I_2 = 100\text{ A} \rightarrow 50\text{ A}$ ($1\text{ A}/\mu s$ slew rate), $P_2 = 5\text{ kW}$.

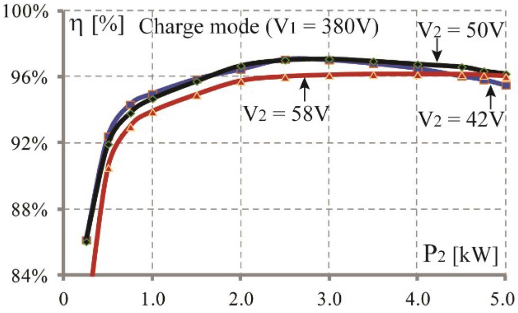

Fig. 20. Efficiency measurements in charge mode operation. Test conditions: $\boldsymbol{V}_1 = 380\text{ }\mathbf{V}$, $\boldsymbol{V}_2 = (42 \div 58)\text{ }\mathbf{V}$.

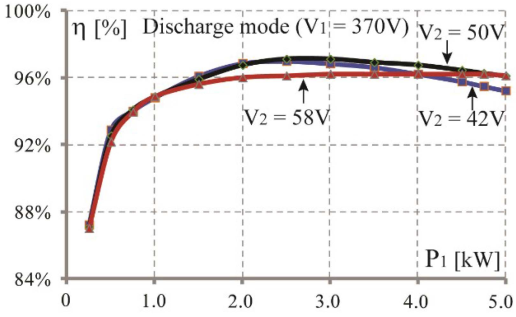

Fig. 21. Efficiency measurements in discharge mode operation. Test conditions: $\boldsymbol{V}_1 = 370\text{ }\mathbf{V}$, $\boldsymbol{V}_2 = (42 \div 58)\text{ }\mathbf{V}$.

V. CONCLUSION

This article presented the research and development of a new DAB-based energy storage converter architecture, which allows parallel and series LV-bridge configurations. The dc port comprised of two LV-bridges allows flexibility in operation through a specific switch arrangement. Therefore, DAB-based augmented with a switch structure doubles the voltage utilization range, enabling a wide range of applications for batteries (e.g., 48-V, 120-V or accordingly scaled for higher voltages). A comparison between the DAB-based converter and the conventional DAB converter has been provided through a graphical approach.

The research continued with the converter's switching key waveforms investigation through harmonics analysis and the evaluation of two different transformer designs. The performance of the typical copper-foil transformer used in high current magnetics has been compared with a new transformer construction. The emergence of capacitive transformer coupling between primary, and secondary has been reduced by five times thanks to the windings layer disposition and three-layer shield design. The proposed wire-wound shielded transformer design used in the two parallel LV-bridges and series HV-bridge demonstrated improved performance with respect to common-mode current circulation and electromagnetic compatibility. The stray capacitance has been reduced through the arrangement of the cooling heatsinks and the three-layer shield transformer design for leakage current mitigation and increased soft-switching range. The analysis continued with the comparisons between hard-switching and soft-switching power devices operation at lower power operation, as being the worst-case scenarios of the DAB-based converter operation.

Finally, the proposed DAB-based converter topology and design with high dc gain and power capability provides an attractive solution for energy storage applications.

REFERENCES

[1] R. W. A. A. De Doncker, D. M. Divan, and M. H. Kheraluwala, "A three-phase soft-switched high-power-density DC/DC converter for high-power applications," *IEEE Trans. Ind. Appl.*, vol. 27, no. 1, pp. 63–73, Jan./Feb. 1991.

[2] B. Zhao, Q. Song, W. Liu, and Y. Sun, "Overview of dual-active-bridge isolated bidirectional DC–DC converter for high-frequency-link power-conversion system," *IEEE Trans. Power Electron.*, vol. 29, no. 8, pp. 4091–4106, Aug. 2014.

[3] F. Krismer and J. Kolar, "Closed form solution for minimum conduction loss modulation of DAB converters," *IEEE Trans. Power Electron.*, vol. 27, no. 1, pp. 174–188, Jan. 2012.

[4] A. Tong, L. Hang, G. li, X. jiang, and S. Gao, "Modeling and analysis of dual-active-bridge isolated bidirectional DC/DC converter to minimize rms current with whole operating range," *IEEE Trans. Power Electron.*, vol. 33, no. 6, pp. 5302–5316, Jun. 2018.

[5] N. Hou, W. Song, and M. Wu, "Minimum-current-stress scheme of dual active bridge DC–DC converter with unified phase-shift control," *IEEE Trans. Power Electron.*, vol. 31, no. 12, pp. 8552–8561, Dec. 2016.

[6] H. Shi, H. Wen, J. Chen, Y. Hu, L. Jiang, and G. Chen, "Minimum-reactive-power scheme of dual-active-bridge DC–DC converter with three-level modulated phase-shift control," *IEEE Trans. Ind. Appl.*, vol. 53, no. 6, pp. 5573–5586, Nov./Dec. 2017.

[7] A. Tong, L. Hang, G. Li, X. Jiang, and S. Gao, "Modeling and analysis of a dual-active-bridge-isolated bidirectional DC/DC converter to minimize RMS current with whole operating range," *IEEE Trans. Power Electron.*, vol. 33, no. 6, pp. 5302–5316, Jun. 2018.

[8] J. Huang, Y. Wang, Z. Li, and W. Lei, "Unified triple-phase-shift control to minimize current stress and achieve full soft-switching of isolated bidirectional DC–DC converter," *IEEE Trans. Ind. Electron.*, vol. 63, no. 7, pp. 4169–4179, Jul. 2016.

[9] F. Zahin, A. Abasian, and S. A. Khajehoddin, "An alternative dual active bridge modulation to minimize RMS current and extend ZVS range," in *Proc. IEEE Energy Convers. Congr. Expo.*, 2020, pp. 5952–5959.

[10] M. Rolak, C. Sobol, M. Malinowski, and S. Stynski, "Efficiency optimization of two dual active bridge converters operating in parallel," *IEEE Trans. Power Electron.*, vol. 35, no. 6, pp. 6523–6532, Jun. 2020.

[11] H. Zhou, T. Duong, S. T. Sing, and A. M. Khambadkone, "Interleaved bi-directional dual active bridge DC-DC converter for interfacing ultracapacitor in micro-grid application," in *Proc. IEEE Int. Symp. Ind. Electron.*, 2010, pp. 2229–2234.

[12] C. Luo and S. Huang, "Novel voltage balancing control strategy for dual-active-bridge input-series-output-parallel DC-DC converters," *IEEE Access*, vol. 8, pp. 103114–103123, 2020.

[13] N. Hou and Y. Li, "The comprehensive circuit-parameter estimating strategies for output-parallel dual-active-bridge DC–DC converters with tunable power sharing control," *IEEE Trans. Ind. Electron.*, vol. 67, no. 9, pp. 7583–7594, Sep. 2020.

[14] B. Zhao, Q. Song, W. Liu, G. Liu, and Y. Zhao, "Universal high-frequency-link characterization and practical fundamental-optimal strategy for dual-active-bridge DC-DC converter under PWM plus phase-shift control," *IEEE Trans. Power Electron.*, vol. 30, no. 12, pp. 6488–6494, Dec. 2015.

[15] C. Jung and D. Lee, "Decoupling control of input-paralleled system with dual active bridge converters," in *Proc. Int. Symp. Elect. Electron. Eng.*, 2019, pp. 226–231.

[16] B. Zhao, Q. Song, J. Li, Y. Wang, and W. Liu, "Modular multilevel high-frequency-link DC transformer based on dual active phase-shift principle for medium-voltage DC power distribution application," *IEEE Trans. Power Electron.*, vol. 32, no. 3, pp. 1779–1791, Mar. 2017.

[17] Z. Zhang, K. Tomas-Manez, Y. Xiao, and M. A. E. Andersen, "High voltage gain dual active bridge converter with an extended operation range for renewable energy systems," in *Proc. IEEE Appl. Power Electron. Conf. Expo.*, 2018, pp. 1865–1870.

[18] E. Serban, C. Pondiche, J. Wassmuth, and M. Ordonez, "Bidirectional parallel low-voltage series high-voltage DAB-based converter analysis and design," in *Proc. IEEE Appl. Power Electron. Conf. Expo.*, 2022, pp. 107–114.

[19] E. Serban, C. Pondiche, and M. Ordonez, "DAB-based energy storage system with flexible voltage configuration and extended power capability," in *Proc. IEEE Appl. Power Electron. Conf. Expo.*, Mar. 2023.

[20] G. Buticchi, D. Barater, L. F. Costa, and M. Liserre, "A PV-inspired low-common-mode dual-active-bridge converter for aerospace applications," *IEEE Trans. Power Electron.*, vol. 33, no. 12, pp. 10467–10477, Dec. 2018.

[21] Y. Yan, Y. Huang, R. Chen, and H. Bai, "Building common-mode analytical model for dual active bridge incorporating with different modulation strategies," *IEEE Trans. Power Electron.*, vol. 36, no. 11, pp. 12608–12619, Nov. 2021.

[22] E. Serban, C. Pondiche, and M. Ordonez, "Modulation effects on power-loss and leakage current in three-phase solar inverters," *IEEE Trans. Energy Convers.*, vol. 34, no. 1, pp. 339–350, Mar. 2019.

[23] H. Geramirad et al., "Conducted EMI reduction in a 100kW 1.2kV Dual Active Bridge converter," in *Proc. PCIM Europe Digit. Days, Int. Exhib. Conf. Power Electron., Intell. Motion, Renewable Energy Energy Manage.*, Germany, 2020, pp. 1–8.

[24] Y. Xiao, Z. Zhang, and M. A. E. Andersen, "Power flow models of GaN based partial parallel dual active bridge (P2DAB) DC-DC converter," in *Proc. IEEE Int. Power Electron. Appl. Conf. Expo.*, 2018, pp. 1–7.

[25] A. K. Bhattacharjee and I. Batarseh, "Optimum hybrid modulation for improvement of efficiency over wide operating range for triple-phase-shift dual-active-bridge converter," *IEEE Trans. Power Electron.*, vol. 35, no. 5, pp. 4804–4818, May 2020.

[26] B. Zhao, Q. Song, and W. Liu, "Efficiency characterization and optimization of isolated bidirectional DC–DC converter based on dual-phase-shift control for dc distribution application," *IEEE Trans. Power Electron.*, vol. 28, no. 4, pp. 1711–1727, Apr. 2013.

[27] E. Serban, M. A. Saket, and M. Ordonez, "High performance gate-driver power supply for multilevel-based 1500 V converters," in *Proc. IEEE Energy Convers. Congr. Expo.*, 2020, pp. 3163–3170.

[28] E. Serban, M. A. Saket, and M. Ordonez, "High-performance isolated gate-driver power supply with integrated planar transformer," *IEEE Trans. Power Electron.*, vol. 36, no. 10, pp. 11409–11420, Oct. 2021.

Emanuel Serban (Senior Member, IEEE) received the B.Sc. and M.Sc. degrees in electrical engineering from Polytechnic University of Timisoara, Timisoara, Romania, in 1994 and 1995, respectively, and the Ph.D. degree in electrical and computer engineering from the University of British Columbia, Vancouver, Canada, in 2007.

In 1997, he was with Xantrex Technology Inc., where he developed several power electronics platforms, e.g., programmable power supplies and energy storage systems. From 2009 to 2019, he was with the Solar Business at Schneider Electric, Canada, as Research and Development Chief Engineer, Power Electronics Design, responsible for hybrid distributed power systems, renewable multilevel converters architecture, and platform design.

He is currently an adjunct Professor with the Department of Electrical and Computer Engineering, University of British Columbia. Additionally, he holds a position in the industry as an R&D Power Conversion Engineering Manager with EnerSys. He specializes in research and development of single-phase and three-phase converter platforms for residential, commercial, and industrial solutions in solar and energy applications. He is the holder of several patents in photovoltaic and energy storage systems. His main research interests include power electronics modeling and control, analysis and design of power converters for renewable, storage, and distributed energy systems.

Dr. Serban was the recipient of with the best IEEE Power Electronics Society Ph.D. Thesis prize.

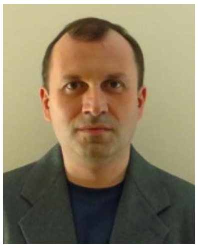

Cosmin Pondiche (Member, IEEE) received the B.Sc. and M.Sc. degrees in electrical engineering from the University Politehnica of Timisoara, Timisoara, Romania, in 1994 and 1995, respectively.

In 1999, he was with the Alpha Technologies Inc., Vancouver, Canada, and his research and development were in advanced switch mode power electronics for UPS and renewable products. From 2010 to 2020, he was with the Renewable Energies Business with Schneider Electric, Vancouver, BC, Canada, where he was a Senior Power Electronics Design/Research Engineer. He currently is Principal Power Electronics Engineer with EnerSys, where he develops power conversion solutions for telecommunications applications. His current research interests include power electronics modeling and control, analysis and design of power converters for renewable, storage, and distributed energy systems.

Martin Ordonez (Member, IEEE) is a Professor and Canada Research Chair in Power Converters for Renewable Energy Systems with the Department of Electrical and Computer Engineering, University of British Columbia, Vancouver, BC, Canada. He is also the holder of the Fred Kaiser Professorship on Power Conversion and Sustainability at UBC. He was an adjunct Professor with Simon Fraser University, Burnaby, BC, Canada, and Memorial University of Newfoundland, St. John’s, NL. His industrial experience in power conversion includes research and development with Xantrex Technology Inc./Elgar Electronics Corporation (now AMETEK Programmable Power in San Diego, California). With the support of industrial funds and the Natural Sciences and Engineering Research Council, he has contributed to more than 190 publications and R&D reports. He participated in panels and evaluation groups for NSERC, NSF, Ontario Research Funds, United Nations Canada, MITACS.

Dr. Ordonez is an Associate Editor of the IEEE TRANSACTIONS ON POWER ELECTRONICS, IEEE JOURNAL OF EMERGING AND SELECTED TOPICS IN POWER ELECTRONICS, and Editor for IEEE TRANSACTIONS ON SUSTAINABLE ENERGY. He is with several IEEE committees, and reviews widely for IEEE/IET journals and international conferences.